energies

MDPI

Article

Perovskite Solar Cell with Added Gold/Silver Nanoparticles: Enhanced Optical and Electrical Characteristics

Ali Hajjiah [1,*], Hussein Badran [1], Ishac Kandas [2,3,†] and Nader Shehata [2,3,4,†]

1 Department of Electrical Engineering, College of Engineering and Petroleum, Kuwait University, Safat 13133, Kuwait; badran.hussein23@gmail.com
2 Department of Engineering Mathematics and Physics, Faculty of Engineering, Alexandria University, Alexandria 21544, Egypt; ishac@vt.edu (I.K.); n.shehata@kcst.edu.kw (N.S.)
3 Kuwait College of Science and Technology, Doha Area, 7th Ring Road, Safat 13133, Kuwait
4 USTAR Bio-Innovation Center, Utah State University, Logan, UT 84341, USA
* Correspondence: ali.hajjiah@ku.edu.kw; Tel.: +965-9966-2234
† These authors contributed equally to paper.

Received: 22 June 2020; Accepted: 8 July 2020; Published: 28 July 2020

Abstract: Different perovskite materials, such as methylammonium lead triiodide $MAPbI_3$, exhibit many outstanding and desirable properties in solar energy harvesting. In this paper, the enhancement of perovskite solar cells' both optical and electrical characteristics through adding either gold (Au) or silver (Ag) nanoparticles (NPs) using different simulations was studied. The used plasmonic nanoparticles were found to be able to compensate for the low absorption of $MAPbI_3$ in the visible with optical coupling resonance frequencies close to that spectrum. Optimal diameters of Au and Ag NPs were found and simulated, and their impact on different parameters such as transmission, absorption, reflection, external quantum efficiency (EQE), open circuit voltage, short-circuit current density, fill factor, and most importantly, efficiency of the perovskite solar cell, have been investigated.

Keywords: plasmonic nanoparticles; perovskite; solar cell; absorption; quantum efficiency

1. Introduction

Solar photovoltaic (PV) is one of the world's best renewable energy sources, having experienced exponential growth over the last several years [1], with an expected installed capacity of 1 terawatt (TW) by 2022–2023 [2]. One prominent emerging type of solar cells is perovskite solar cells. Even though perovskites had a weak start in photovoltaic applications in 2009, with power conversion efficiency as little as 3.8% [3], their efficiencies have skyrocketed to 14% in 2013 and to ~23% in 2018 [4]. Additionally, as of June 2018, thin-film perovskite technologies have exceeded all other thin-film solar cell technologies, including cadmium telluride (CdTe) and Copper Indium Gallium Selenide (CIGS), proving to be a strong candidate to the future of solar PV.

One of the most promising perovskite materials is methylammonium lead triiodide ($MAPbI_3$ or MAPI), exhibiting many outstanding and desirable properties. Its electrical properties include: a direct bandgap [5] with a value around 1.6 eV with shallow defect levels [6], tunable bandgap (up to 2.25 eV) [7], a large open circuit voltage of 1.07 [8], and a relatively high short-circuit current density. Not only does $MAPbI_3$ excel electrically, but it also possesses some appealing optical properties, such as high carrier mobilities [9], high absorption coefficient [10,11], and long diffusion lengths [12–14]. All these exceptional and advantageous properties are important metrics for high performance solar cells [15], making $MAPbI_3$ one of the top contenders in perovskite solar cell technology.

One of the ways to enhance the performance of perovskite solar cells is by the addition of plasmonic NPs to the cell. Plasmonic NPs, known for their very useful and interesting properties, have become the subject of many scientific applications over the past decade [16]. More importantly, metallic NPs have attracted the most attention due to their optical properties, allowing their applications to vary from biology, to photothermal imaging and therapy, to solar cells and much more. Many metallic NPs exhibit high absorption in the visible electromagnetic spectrum range, but only Au, Ag, and copper (Cu) NPs exhibit surface plasmon resonance (SPR) effect in that visible region too [16]. SPR is a phenomenon in which polarized light hits a metallic film at the interface of media with different refractive indices which causes the collective oscillation of free electrons, known as surface plasmons. These plasmons can be set to resonate with light, resulting in high absorption of light [17]. This SPR effect is particularly effective in solar cell applications due to the great absorption of light NPs have to offer, especially Au and Ag. This improvement in absorption can lead to an improved power conversion efficiency which we aspire to achieve. Over the last few years, there have been some recent experimental works of embedding plasmonic nanostructures, such as both Ag and Au NPs, within perovskite solar cells to enhance the power conversion efficiency (PCE). The experimental synthesized plasmonic-perovskite cell improved PCE from 15.4% up to 17.3% when adding both blended Ag and Au nanocrystals of 1 vol.%. However, the design technique is still dependent on blending the plasmonic nanocrystals within the perovskite layer of the cell [18–20].

In this paper, the enhancement of perovskite solar cells through the addition of Au and Ag NPs is studied. This enhancement is analyzed both optically and electrically. Our aim is to demonstrate the effect of these NPs to the optical and electrical characteristics of the cell through different simulations. It is shown that plasmonic NPs are able to compensate for the low absorption of $MAPbI_3$ in the visible spectrum by adding NPs with resonance frequencies close to that spectrum [15]. Optimal diameters of Au and Ag NPs are found and simulated, and their impact on different parameters such as transmission, absorption, reflection, external quantum efficiency (EQE), open circuit voltage (V_{oc}), short-circuit current density (J_{sc}), fill factor (FF), and most importantly, efficiency (η) of the perovskite solar cell, is investigated. Through our work, the plasmonic layer of NPs is added to the rear side of the solar cell. That configuration is proven to be more effective in enhancing the photocurrent [21,22].

2. Theoretical Modeling

2.1. Optical Modeling

Stanford University McGehee Group's Transfer Matrix Optical Modeling software was used to optically simulate and model our cell. The software utilizes the transfer matrix method (TMM) which solves Maxwell's equations at the layers' interfaces to optically model the thin-film layer stacks [23]. Stanford's TMM code uses complex refractive index and the thickness of each layer as input, and outputs the absorbance, reflectance, electric field intensity, and photogeneration rate of each layer, along with the overall optical short circuit current density.

2.2. Silvaco TCAD-ATLAS (Electrical Modeling)

A Silvaco ATLAS technology computer-aided design (TCAD) simulation was used to model the electrical behavior of our cell. ATLAS is a 2D and 3D device simulator based on finite element analysis that performs DC, AC, and transient analysis for numerous material-based devices and enabling the characterization and optimization of semiconductor devices for a wide range of technologies [24]. Its working principle is based on solving Poisson's equations, charge carrier continuity equations, and charge transport of drift-diffusion equations for electrons and holes [25,26]; allowing the generation of the desired J–V curves and the extraction of: J_{sc}, V_{oc}, FF, and the η of the cell.

3. Case Study

The cell under study is a semitransparent perovskite solar cell with an n-i-p architecture: TCO/ETL/Perovskite/HTL/TCO. For the transparent conductive oxide (TCO), a 140 nm thick indium–tin oxide (ITO)-coated glass substrate as front electrode and 50 nm thick ITO as the back electrode. The electron transport layer (ETL) consists of 5 nm thick SnO_2 combined with 15 nm thick phenyl-C61-butyric acid methyl ester (PCBM) bilayer. The perovskite material used in this study is a 372 nm thick $MAPbI_3$ followed by a 250 nm thick 2,2′,7,7′-tetrakis[N,N-di(4-methoxyphenyl)amino]-9,9′-spirobifluorene (Spiro-OMeTAD) as hole transport layer (HTL). Roughness layers for front ITO, $MaPbI_3$, and rear ITO were added to simulate experimental irregularities with thicknesses of 4 nm, 50 nm, and 10 nm, respectively. Both Au and Ag NPs will be applied to the rear of the perovskite solar cell, and their effect on the performance of the solar cell will be studied both optically and electrically. The model of the cell is illustrated in the schematic in Figure 1.

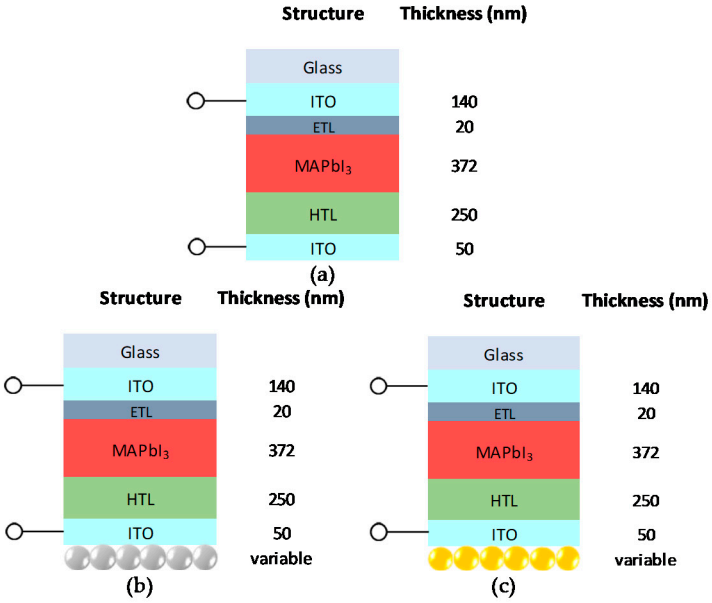

Figure 1. (**a**) Model of the semitransparent cell structure. (**b**) Model of the cell structure with added Ag NPs. (**c**) Model of the cell structure with added Au NPs.

4. Simulation Procedure

The optical and electrical simulations are mainly focused on studying the effect of adding either Au or Ag NPs to the rear end of a semitransparent perovskite solar cell. The optical simulation started by using the Effective Medium Theory (EMT) to approximate the NP spheres and represent them with a planar stack of changing refractive index. Then, the TMM was used with the derived effective refractive index from EMT to represent the Au and Ag NPs. In the TMM, the diameters of these NPs were varied in order to find the optimum thickness which yields the highest optical J_{sc}. Photogeneration files corresponding to the optimum NPs thickness from the optical TMM simulations were used in the electrical simulation via Silvaco ATLAS to investigate the effect of Au and Ag NPs on the electrical performance of the perovskite solar cell.

4.1. Optical Simulation

4.1.1. Planarization of the Au and Ag NPs Using EMT Method

The EMT was used to model NPs at the rear side of our cell. Being suspended at the rear of the cell, these nanospheres form a graded refractive index at the air/NP interface from either side. For periods smaller than $\lambda/(2n)$, n being the refractive index of the NP, the propagation of light can be

explained using the EMT [27,28] by approximating the spheres and representing them with a planar stack of changing refractive index [29], as shown in Figure 2.

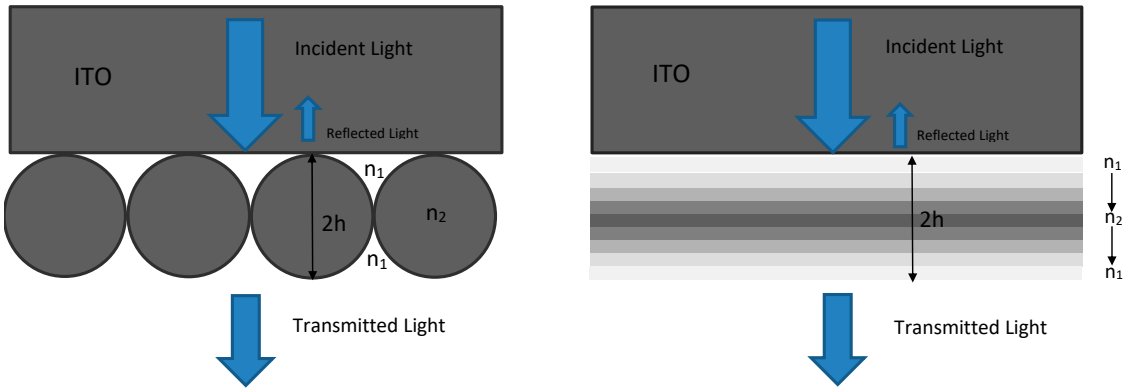

Figure 2. EMT representation of the nanospheres as a planar stack of changing refractive index.

The effective refractive index of each of the layers can be expressed by the following formula, Equation (1) [30]:

$$n_{eff}(z) \approx n_2 \cdot f(z) + n_1 \cdot (1 - f(z)) \quad (1)$$

where n_1 and n_2 are the refractive indices of the incident medium and the metallic NPs, respectively, and *f(z)* being the volume ratio as a function of the height of the structure, z. The volume ratio can be expressed as $f(z) = A_n(z)/A_{grid}$, where A_{grid} is the area of the nanospheres arrangement grid, which is circular in our case, and $A_n(z)$ is the cross-sectional area of the sphere at a height z. Hence, the effective refractive index, Equation (1), can be simplified to Equation (2):

$$n_{eff}(z) \approx n_2 \cdot \frac{A_n(z)}{A_{grid}} + n_1 \cdot \left(\frac{A_{grid} - A_n(z)}{A_{grid}} \right) \quad (2)$$

with $A_{grid} = \pi r_b^2$ and $A_n(z) = A_{base} \cdot AHF(z) = \pi r_b^2 \cdot AHF(z)$, where r_b is the base radius of the grid and *AHF(z)* being the area height factor, ranging from 0 to 1. By substituting, a generalized formula for the effective refractive index with a circular grid is derived and expressed in Equation (3):

$$n_{eff}(z) \approx AHF(z) \cdot (n_2 - n_1) + n_1 \quad (3)$$

For spheres, see Figure 3, it was derived that the $AHF(z) = 1 - \left(\frac{z}{h}\right)^2$, with h being the height or half the thickness of the sphere, yielding a final expression for effective refractive index for spheres, Equation (4):

$$n_{eff,sphere}(z) \approx \left(1 - \left(\frac{z}{h}\right)^2\right) \cdot (n_2 - n_1) + n_1, \quad h \le z \le -h \quad (4)$$

Utilizing the equation above (Equation (4)), we converted each sphere into a one-dimensional multilayer stack in the z-direction. The effective refractive index of the stacks was varied according to the equation, from $z = h$, the top of the sphere, to $z = -h$, the bottom of the sphere; see Figure 3. This resulted in an effective sweep of the refractive index, from n_{air} ($z = h$) to n_{Au} and n_{Ag} at the base of the sphere ($z = 0$), and back to n_{air}, at the bottom of the sphere ($z = -h$), for each structure. A plot of normalized height versus effective refractive index shows the refractive index profile of the graded index for both Au and Ag NPs; see Figure 4.

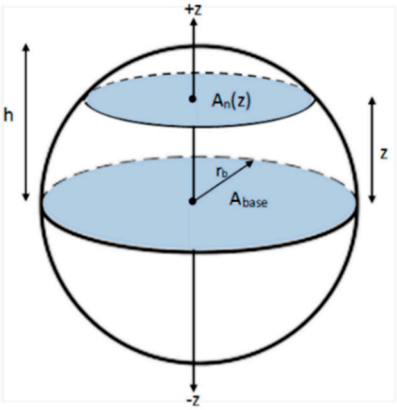

Figure 3. Nanosphere representation with relevant EMT parameters.

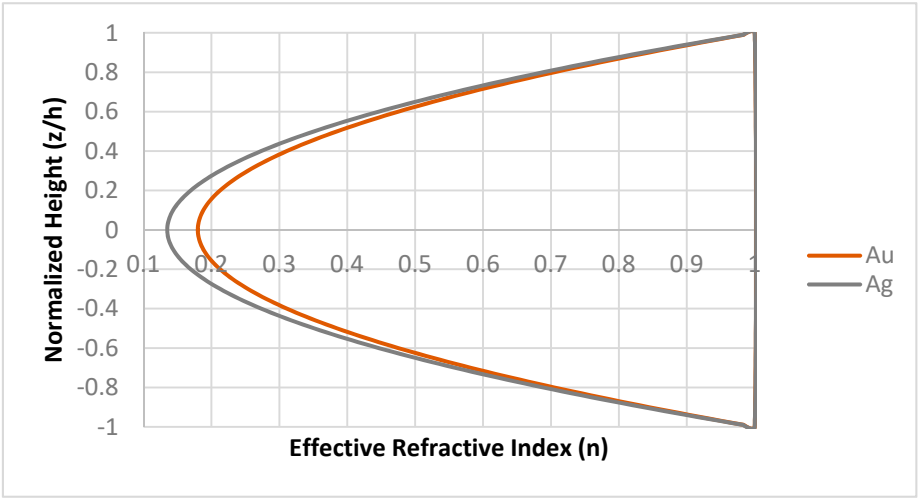

Figure 4. Normalized height vs. effective refractive index for both Au and Ag nanospheres.

4.1.2. Optimization of the Au and Ag NPs Size Using TMM

This part of the optical simulation was performed using the Stanford TMM MATLAB code, where the layers were added as shown in the schematic of Figure 1. The complex refractive index of each material was added to the software's refractive index library file and renamed accordingly. All the complex refractive index values were obtained from literature and referenced [31–35]. The thickness of each layer was also set according to Figure 1. To obtain precise and accurate results, the wavelength range was set from 300 nm to 1200 nm with a small step size increment of 1 nm. $MAPbI_3$ was selected as the active material in the cell, where photocurrent will be generated.

To find the optimum thickness for the Au and Ag NPs, the diameter was swept from 0 to 300 nm and the optical J_{sc} was observed and recorded for each thickness. Figure 5 shows the diameter optimization for Au and Ag NPs. A maximum J_{sc} of 20.25 mA/cm^2 was reached at a diameter size of 153 nm for the Au nanospheres. For Ag, a higher J_{sc} of 20.38 mA/cm^2 was reached at a lower nanosphere size of 135 nm. Furthermore, photogeneration plots and files, versus the depth of the perovskite material were created at each of these optimum Au and Ag diameters, as seen in Figure 6. It can be seen that the cells with the Au and Ag nanospheres mostly have higher photogeneration rates throughout the depth of the MAPI material than the semitransparent cell, with the Ag cell slightly outperforming the Au cell at certain depths.

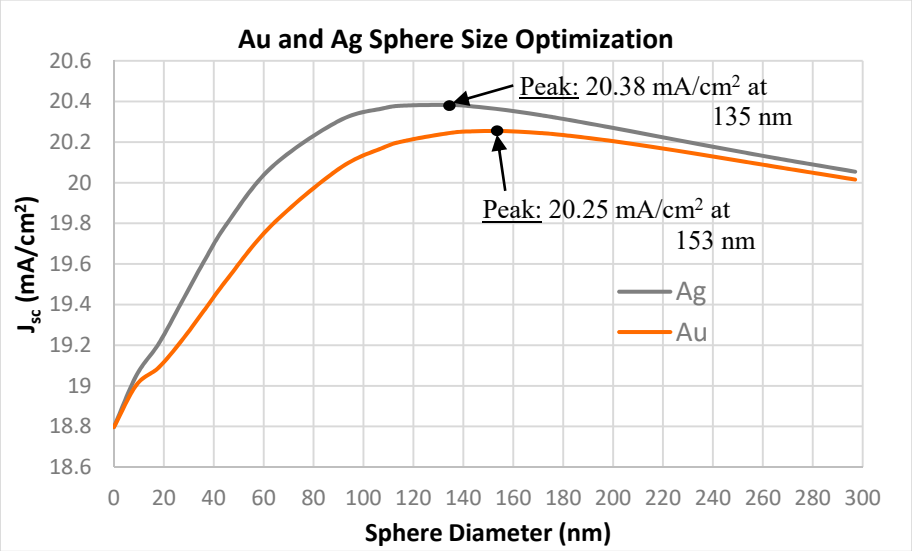

Figure 5. Solar cell J_{sc} vs. Ag and Au nanosphere diameter, indicating the peak for each.

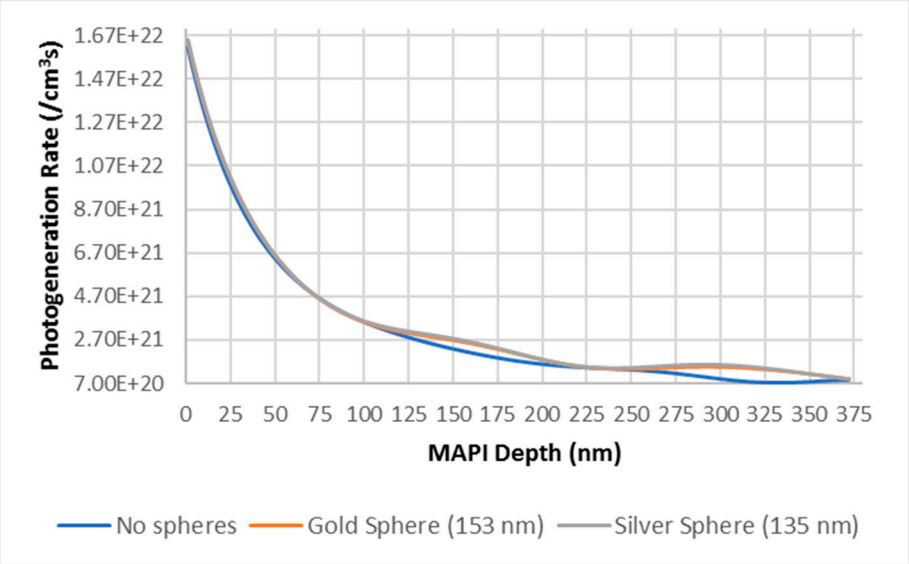

Figure 6. Solar cell generation rate vs. MAPI layer depth for the cell with and without Au and Ag NPs.

4.2. Electrical Simulation

The electrical simulations were performed using Silvaco ATLAS. The device dimensions were first meshed accordingly and optimized to yield the most accurate results. Next, the material layers were added as to the previous suggested structure and doped accordingly. Material parameters were specified for each material according to Table 1 [36–38], selected and cited from experimental and theoretical data. Recombination models were then set for the ETL, HTL, and the perovskite. These models are essential to correctly model the behavior of the cell, especially when we have both organic and inorganic materials in the cell, which is why Silvaco ATLAS was chosen to accurately model and simulate our cell. For the ETL, the carrier concentration dependent mobility and Shockley–Read–Hall (SRH) recombination were set. For the perovskite, the Poole–Frankel field dependent mobility model, SRH, and Langevin recombination were set. As for the HTL, the Poole–Frankel field dependent mobility model and Langevin recombination were specified, as found in the literature [39]. The photogeneration rate from the optical TMM simulation was then used as an input file. With this file, ATLAS can perform all the necessary calculations and solve all the equations necessary to extract the required electrical

parameters. Silvaco ATLAS was then finally ready to solve the solar cell. The voltage was swept from 0 to 1.1 V with increments of 0.01 V to ensure accuracy. It then extracted all the required electrical parameters including V_{oc}, J_{sc}, FF, and η.

To ensure the reliability of the simulator, a series of calibration simulations were first performed to match the experimental results of a semitransparent perovskite solar cell provided by the Interuniversity Microelectronics Centre (IMEC) [40]. Figure 7 shows the simulated IV curve closely matched with the experimental curve with some small deviation. The electrical parameters extracted from both simulated and experimental IV curves as shown in Table 2. From the table, you can see a strong agreement between the simulated and experimental results.

Table 1. Electronic parameters of the solar cell materials used in ATLAS.

Parameters	SnO_2	PCBM	$MAPbI_3$	Spiro-OMETAD
bandgap (eV)	3.6	2.1	1.55	3.0 [42]
electron affinity (eV)	4.5	3.9	3.8	2.45 [42]
dielectric permittivity (relative)	9.0	3.9	6.5 [41]	3.0 [42]
CB effective density of states ($1/cm^3$)	2.20×10^{18}	2.20×10^{19}	1.00×10^{19}	2.00×10^{18} [43]
VB effective density of states ($1/cm^3$)	1.80×10^{19}	2.20×10^{19}	1.00×10^{17}	2.00×10^{19}
electron mobility (cm^2/Vs)	1.00×10^{2}	1.00×10^{-3}	1.00×10^{0}	2.00×10^{-3}
hole mobility (cm^2/Vs)	2.50×10^{1}	2.00×10^{-3}	1.00×10^{0}	2.00×10^{-3}
electron lifetime (s)	1.00×10^{7}	1.00×10^{-7}	1.00×10^{-6}	1.00×10^{-7}
hole lifetime (s)	1.00×10^{7}	1.00×10^{-7}	1.00×10^{-6}	1.00×10^{-7}
uniform donor density ND ($1/cm^3$)	5.635×10^{17}	5.6350×10^{19}	1.00×10^{13}	0.00×10^{0}
uniform acceptor density NA ($1/cm^3$)	0.00×10^{0}	0.00×10^{0}	0.00×10^{0}	1.00×10^{17}

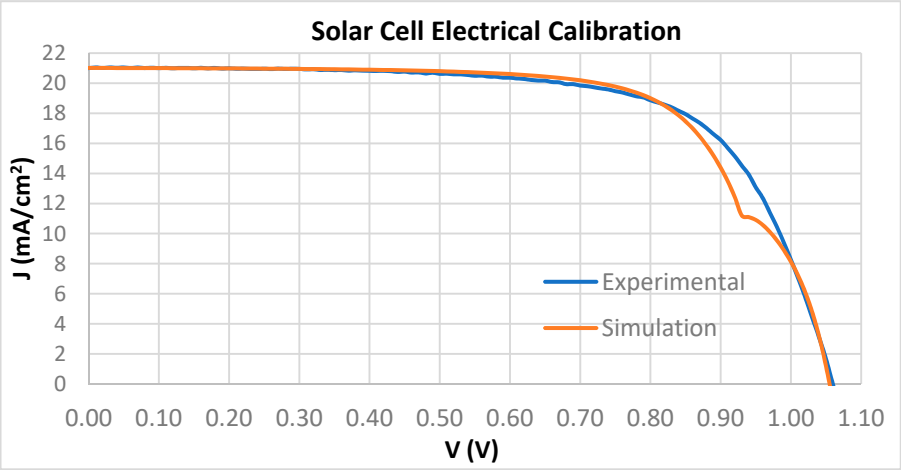

Figure 7. J–V curves of experimental and simulated solar cell.

Table 2. Comparison of electric parameters between experimental and simulated cells.

	V_{oc} (V)	J_{sc} (mA/cm^2)	FF (%)	η (%)
Experimental	1.060	21.01	68.60	15.300
Simulation	1.055	21.01	68.61	15.209

5. Results and Discussion

With the simulator calibrated, J–V curves were produced for our semitransparent cell with and without the optimally sized Au and Ag NPs. Figure 8 show a comparison between the three J–V curves along with a summary of the extracted electrical parameters in Table 3. It is clear that the added NPs have a direct effect on the enhancement of the J_{sc}, with an increase of 1.45 mA/cm^2 and 1.58 mA/cm^2 for Au and Ag NPs, respectively. This may be due to the improvement in the EQE

of the cell. However, this had minimal-to-negligible effect on V_{oc}; which almost remained constant. The FF, however, decreased, as expected, by ~1% with the addition of the Au and Ag NPs at the rear side. This can be explained due to the increased value of the cell's sheet resistance. Overall, an improvement of ~1% on the conversion efficiency was achieved by adding either Au or Ag NPs at the rear-side of a semitransparent $MAPbI_3$ perovskite solar cell with Ag slightly outperforming Au.

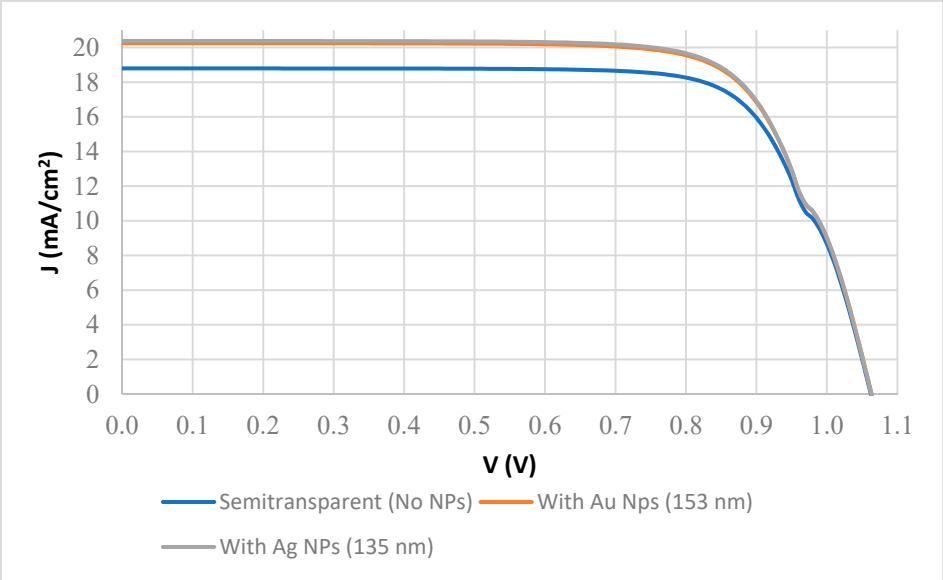

Figure 8. J–V curves of the semitransparent solar cell and the cell with the added Ag and Au NPs at optimized diameters.

Table 3. Comparison of the electric parameters of the semitransparent cell with no NPs and with Au and Ag NPs.

Structure	J_{sc} (mA/cm^2)	V_{oc} (V)	FF (%)	η (%)
Semitransparent Cell (No NPs)	18.80	1.06	74.93	14.96
With Au NPs (153 nm)	20.25	1.06	74.03	15.94
With Ag NPs (135 nm)	20.38	1.06	73.97	16.03

To further investigate the reason behind the slight improvement in performance of Ag NP over the Au NP, and to gain a clear-cut understanding, three optical analyses are considered in this paper:

5.1. Solar-Weighted Reflectance

The solar-weighted reflectance (SWR) is a measure of reflectivity over the entire solar spectrum weighted by the intensity of sunlight of each wavelength. Since the reflection plots produced were a function of wavelength, it is sometimes difficult to determine which reflection curve results in lower or higher overall reflection. The SWR provides a more tangible measure of reflectance by providing a single numerical expression for the reflectance rather than a function of wavelength. It is expressed in Equation (5) by the following expression [44]:

$$\mathrm{SWR} = 1 - \frac{\int_{\lambda_1}^{\lambda_2} (1 - \mathrm{R}(\lambda)) \cdot \varphi_{\mathrm{AM\ 1.5G}}(\lambda) \cdot \mathrm{d}\lambda}{\int_{\lambda_1}^{\lambda_2} \varphi_{\mathrm{AM\ 1.5G}}(\lambda)\ \cdot \mathrm{d}\lambda} \tag{5}$$

where λ is the wavelength, $R(\lambda)$ is the reflection of the cell, and $\varphi_{AM\ 1.5G}$ is the AM1.5G solar spectrum. Integrations were performed from 300 nm to 800 nm, which is the interval of interest in our perovskite solar cell. A summary of the results is provided in Table 4. With the SWR calculations, it can be seen

that the addition of the NPs has a clear and significant impact on the overall reflection of the cell, resulting in an increase of ~3.5% with the Au NPs and ~4% with the Ag NPs. This may cause photon recycling, and therefore, increase the probability of absorption in the perovskite layer which causes an increase in the external quantum efficiency of the solar cell. As a result, a slight increase in $J_{sc.}$ with Ag NPs over Au NPs can be seen.

Table 4. SWR data for the three different cell structures.

Structure	SWR (%)
Semitransparent Cell	8.959
Cell with Au NPs	12.505
Cell with Ag NPs	12.931

5.2. Solar Absorptance Enhancement

Similar to SWR, the solar absorptance enhancement (SAE) also provides a better understanding and interpretation of one of the most important optical parameters, absorption. The SAE translates the absorption vs. wavelength into a numeric ratio which indicates the degree in absorption enhancement. The SAE is expressed in Equation (6) by the following expression [45]:

$$\mathrm{SAE} = \frac{\int_{\lambda_1}^{\lambda_2} \mathrm{A_{structure}}(\lambda)\cdot\varphi_{\mathrm{AM\ 1.5G}}\cdot d\lambda}{\int_{\lambda_1}^{\lambda_2} \mathrm{A_{reference}}(\lambda)\cdot\varphi_{\mathrm{AM\ 1.5G}}\cdot d\lambda} \quad (6)$$

where A is the total absorption of the cell (i.e., $A = EQE_{perovskite} + A_{parasitic}$), $\mathrm{A_{reference}}$ represents the absorption of the semitransparent cell with no NPs, whereas $\mathrm{A_{structure}}$ represents the absorption of the cell with the added NPs. A value of SAE > 1 implies a positive effect or an enhancement and SAE < 1 implies a negative effect or a deterioration, whereas SAE = 1 implies no enhancement or deterioration in absorption. Integrations were performed from 300 nm to 800 nm, which is the interval of interest in our perovskite solar cell. Calculations were performed on three different kinds of absorptions: the total cell absorption, perovskite absorption, and parasitic absorption. A summary of the results is provided in Table 5.

Table 5. SAE data for the three different cell structures.

Structure	SAE		
	Total	Perovskite	Parasitic
Semitransparent Cell	1.000	1.000	1.000
Cell with Au NPs	1.154	1.077	1.956
Cell with Ag NPs	1.150	1.084	1.830

With the SAE calculations, it can be seen that the addition of the plasmonic NPs has a clear and significant impact on the overall absorption enhancement of the cell, with Au NPs resulting in just a minor fraction more total absorption enhancement than the Ag NPs. However, this extra absorption is being squandered on parasitic absorption, as the NPs resulted in an SAE value of 1.956 and 1.83 for Au and Ag NPs, respectively. Thus meaning, the Ag NPs contributed more to the perovskite absorption (i.e., EQE), with an SAE value of 1.084 as opposed by 1.077 for the Au NPs, resulting in higher photocurrent; see Figure 9.

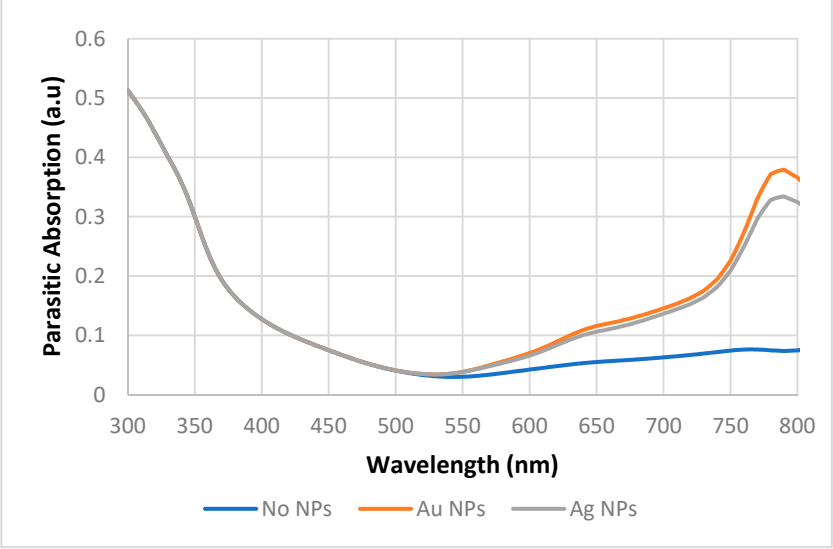

Figure 9. Parasitic absorption plot for the cell with and without Au and Ag NPs.

5.3. Current Density Loss (J_{loss}) Analysis

Reflection, transmission, and absorption are essential parameters that optically characterize a solar cell. They can provide a definite indication on the performance of the cell and ultimately translate into optical current. In order to calculate the current density loss due to reflection, transmission, and parasitic absorption, current loss analysis was carried out to investigate the effect of Au and Ag NPs on the performance of the semitransparent perovskite solar cell, by using TMM simulations. At the device front, part of the light is lost due to external reflection. These reflection losses (i.e., J reflection-loss) are calculated by integrating the reflection spectrum on the front side of the cell according to Equation (7) [15]. Moreover, at the device rear, part of the light is lost due to transmission, where long wavelength light is transmitted through the transparent rear ITO. This external loss is calculated by integrating the transmission curve of the cell according to Equation (8) [15]. Finally, the current loss due to parasitic absorption (i.e., $J_{parasitic\text{-}loss}$) is calculated using Equation (9) [15], by integrating the area between the EQE and the absorbance curves over the AM1.5G solar spectrum for the wavelength region of interest.

$$J_{reflection-loss} = \frac{q}{hc}\int_{300}^{800} \lambda\cdot\Phi(\lambda)\cdot R(\lambda)\cdot d\lambda \left(mA/cm^2\right) \quad (7)$$

$$J_{transmission-loss} = \frac{q}{hc}\int_{300}^{800} \lambda\cdot\Phi(\lambda)\cdot T(\lambda)\cdot d\lambda \left(mA/cm^2\right) \quad (8)$$

$$J_{parasitic-loss} = \frac{q}{hc}\int_{300}^{800} \lambda\cdot\Phi(\lambda)\cdot A_{parasitic}\cdot d\lambda \left(mA/cm^2\right) \quad (9)$$

Furthermore, the total J_{sc} which can be produced by the solar cell for each specific NP can be expressed in Equation (10) as:

$$J_{sc} = \frac{q}{hc}\int_{300}^{800} \lambda\cdot\Phi(\lambda)\cdot EQE(\lambda)\cdot d\lambda \left(mA/cm^2\right) \quad (10)$$

where q is the elementary charge, h is Planck's constant, c is the speed of the light, R is the reflection of the cell, T is the transmission of the cell, and A is the absorption of the cell.

A summary of the results can be found in Table 6. It can be shown that $J_{parasitic} + J_{transmission} + J_{reflection} + J_{sc} = 27.28\ mA/cm^2$ for all structures, which is approximately 27.3 mA/cm^2, the Shockley-Quiesser J_{sc} limit for a 1.55 eV bandgap material [46]. For the semitransparent cell, much of

that current is lost due to transmission losses and only a little is lost due to parasitic absorption and reflection. Adding the Au and Ag seems to mitigate these transmission losses and improve the J_{sc} by 7.76% and 8.44%, respectively; however, the parasitic and reflection losses have also increased unfavorably as depicted by the SWR and SAE calculations. The $J_{reflection}$ increased by ~1 mA/cm^2 and ~1.1 mA/cm^2 while the $J_{parasitic}$ increased by 1.73 mA/cm^2 and 1.5 mA/cm^2 with the addition of Au and Ag NPs, respectively. Overall, the addition of these NPs resulted in a positive impact. J_{sc} also had a direct improvement due to the increase in the EQE of the cell. It should be noted that silver resulted in better overall characteristics than gold with higher absorption, EQE and reflection, along with lower transmission and parasitic absorption. An illustration of these optical parameters can be shown in Figure 10. The magnitude of each parameter is illustrated by the area it covers at its pertinent wavelength region. It can be noticed from Figure 10 that the EQE was also enhanced at wavelength range close to the plasmonic resonance frequency. This enhancement is due to the improvement in the absorption and the entrapment of the reflected photoelectrons [15]. However, the overall parasitic absorption also increased absorption and reflection at the resonance frequency.

Table 6. Current Density Analysis comparison for the three different cell structures.

Structure	Current Density–J (mA/cm^2)				J_{sc} Gain (%)
	J_{losses}			J_{sc}	
	$J_{parasitic}$	$J_{transmission}$	$J_{reflection}$		
Semitransparent Cell	1.80	4.24	2.44	18.80	-
Cell with Au NPs	3.53	0.09	3.41	20.25	7.76
Cell with Ag NPs	3.30	0.07	3.53	20.38	8.44

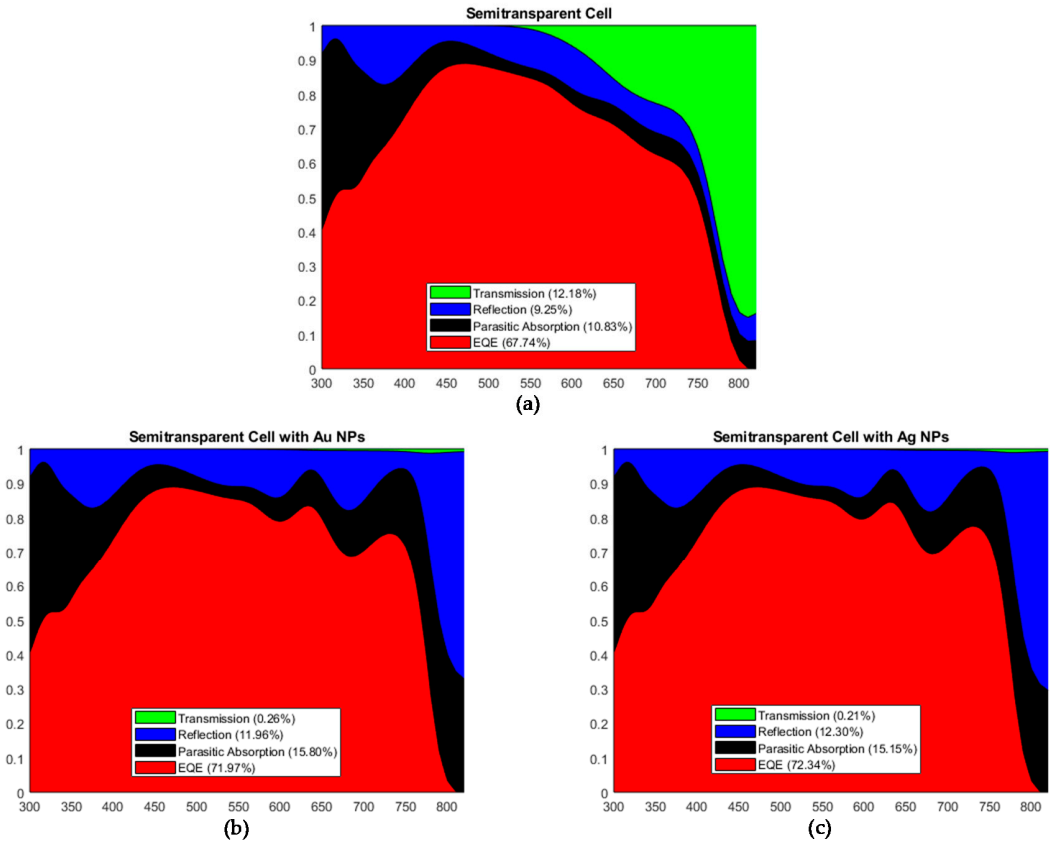

Figure 10. Area plot of the (**a**) semitransparent cell, (**b**) cell with Au NPs, (**c**) cell with Ag NPs, displaying the area covered by the EQE, parasitic absorption, reflection, and transmission.

6. Conclusions

This work shows the enhancement of both optical and electrical properties of a semitransparent perovskite solar cell by the addition of either Au or Ag NPs of different diameters. Optical simulations show that these nanoparticles have improved the external quantum efficiency of the perovskite solar cell at certain parts of the spectrum and in turn, the short-circuit current density. J_{sc} has increased by 1.45 mA/cm^2 (7.76%) and 1.58 mA/cm^2 (8.44%), with the addition of the optimally sized Au and Ag NPs, respectively. On the other hand, electrical simulations showed little-to-no changes in both V_{oc} and FF, but an improvement in the efficiency due to the enhancement of the J_{sc}. The efficiency, η, has increased by ~0.98% and ~1.07% with the addition of the optimally sized Au and Ag NPs, respectively.

Additional optical analysis tools and methods were also considered including: Solar-Weighted Reflectance (SWR), Solar Absorptance Enhancement (SAE), and Current Density Loss (J_{loss}) analysis. SWR calculations show that the overall reflection of the cell increased by ~3.5% with the Au NPs and ~4% with the Ag NPs. SAE calculations show that the Au NPs have increased the total absorption slightly more than the Ag NPs, but this increase was mostly wasted on parasitic absorption rather than the perovskite, unlike the Ag NPs. J_{loss} analysis showed the exact distribution of light in terms of current density. Due to the increase in reflection and parasitic absorption in the cell, $J_{reflection}$ and $J_{parasitic}$ have also increased. The $J_{reflection}$ increased by ~1 mA/cm^2 and ~1.1 mA/cm^2 while the $J_{parasitic}$ increased by 1.73 mA/cm^2 and 1.5 mA/cm^2 with the addition of Au and Ag NPs, respectively. $J_{transmission}$ underwent the biggest improvement, dropping from 4.24 mA/cm^2, down to 0.09 mA/cm^2 and 0.07 mA/cm^2 for Au and Ag NPs, respectively.

Author Contributions: H.B. performed the simulations under the full supervision of A.H. Other members: A.H., N.S. and I.K. contribute in the idea and methodology. A.H. and H.B. wrote the draft version of the paper. A.H., I.K. and N.S. reviewed and edited the paper. N.S. is the main funding investigator (PI), while I.K. and A.H. are Co—PIs. All authors have read and agreed to the published version of the manuscript.

Funding: This project was funded "Fully" by Kuwait Foundation for the Advancement of Sciences (KFAS) under project code: PN18-14SP-01.

Acknowledgments: The authors would like to thank IMEC for providing us with the experimental J–V curves.

Conflicts of Interest: The authors declare no conflict of interest.

References

1. Kurtz, S.; Granata, J.; Quintana, M. Photovoltaic-reliability R&D toward a solar-powered world. In Proceedings of the SPIE 7412, Reliability of Photovoltaic Cells, Modules, Components, and Systems II, 74120Z, San Diego, CA, USA, 20 August 2009.
2. Haegal, N.M.; Atwater, H., Jr.; Barnes, T.; Breyer, C.; Burrell, A.; Chiang, Y.M.; De Wolf, S.; Dimmler, B.; Feldman, D.; Glunz, S.; et al. Terawatt-scale photovoltaics: Transform global energy. *Science* **2019**, *6443*, 836–838. [CrossRef] [PubMed]
3. A decade of perovskite photovoltaics. *Nat. Energy* **2019**, *4*, 1. [CrossRef]
4. NREL Best Research-Cell Efficiencies. 2018. Available online: https://www.nrel.gov/pv/assets/images/best-research-cell-efficiencies.20200406.png (accessed on 3 July 2020).
5. Umebayashi, T.; Asai, K.; Kondo, T.; Nakao, A. Electronic structures of lead iodide based low-dimensional crystals. *Phys. Rev. B* **2003**, *67*, 155405. [CrossRef]
6. Yin, W.J.; Shi, T.; Yan, Y. Unusual defect physics in CH3NH3PbI3 perovskite solar cell absorber. *Appl. Phys. Lett.* **2014**, *104*, 063903. [CrossRef]
7. Noh, J.H.; Im, S.H.; Heo, J.H.; Mandal, T.N.; Seok, S.I. Chemical management for colorful, efficient, and stable inorganic-organic hybrid nanostructured solar cells. *Nano Lett.* **2013**, *13*, 1764–1769. [CrossRef] [PubMed]
8. Liu, M.; Johnston, M.B.; Snaith, H. Efficient planar heterojunction perovskite solar cells by vapour deposition. *Nature* **2013**, *501*, 395–398. [CrossRef]
9. Stoumpos, C.C.; Malliakas, C.D.; Kanatzidis, M.G. Semiconducting Tin and Lead Iodide Perovskites with Organic Cations: Phase Transitions, High Mobilities, and Near-Infrared Photoluminescent Properties. *Inorg. Chem.* **2013**, *52*, 9019–9038. [CrossRef]

10. De Wolf, S.; Holovsky, J.; Moon, S.J.; Löper, P.; Niesen, B.; Ledinsky, M.; Haug, F.; Yum, J.H.; Ballif, C. Organometallic Halide Perovskites: Sharp Optical Absorption Edge and Its Relation to Photovoltaic Performance. *J. Phys. Chem. Lett.* **2014**, *5*, 1035. [CrossRef] [PubMed]
11. Löper, P.; Stuckelberger, M.; Niesen, B.; Werner, J.; Filipic, M.; Moon, S.J.; Yum, J.H.; Topic, M.; DeWolf, S.; Ballif, C. Complex Refractive Index Spectra of CH3NH3PbI3 Perovskite Thin Films Determined by Spectroscopic Ellipsometry and Spectrophotometry. *J. Phys. Chem. Lett.* **2015**, *6*, 66. [CrossRef] [PubMed]
12. Xing, G.; Mathews, N.; Lim, S.; Lam, Y.; Mhaisalkar, S.; Sum, T.C. Long-range balanced electron- and hole-transport lengths in organic-inorganic CH3NH3PbI3. *Science* **2013**, *6960*, 498. [CrossRef] [PubMed]
13. Stranks, S.; Eperon, G.; Grancini, G.; Menelaou, C.; Alcocer, M.; Leijtens, T.; Herz, L.; Petrozza, A.; Snaith, H. Electron-hole diffusion lengths exceeding 1 micrometer in an organometal trihalide perovskite absorber. *Science* **2014**, *342*, 341. [CrossRef]
14. Gonzalez-Pedro, V.; Juarez-Perez, E.; Arsyad, W.; Barea, E.; Fabregat-Santiago, F.; Mora-Sero, I.; Bisquert, J. General working principles of CH3NH3PbX3 perovskite solar cells. *Nano Lett.* **2014**, *14*, 888–893. [CrossRef]
15. Hajjiah, A.; Kandas, I.; Shehata, N. Efficiency Enhancement of Perovskite Solar Cells with Plasmonic Nanoparticles: A Simulation Study. *Materials* **2018**, *11*, 1626. [CrossRef]
16. Boken, J.; Khurana, P.; Thatai, S.; Kumar, D.; Prasad, S. Plasmonic Nanoparticles and Their Analytical Applications: A Review. *Appl. Spectrosc. Rev.* **2017**, *52*, 774–820. [CrossRef]
17. Liang, A.; Liu, Q.; Wen, G.; Jiang, Z. The surface-plasmon-resonance effect of nanogold/silver and its analytical applications. *TrAC Trends Anal. Chem.* **2012**, *37*, 32–47. [CrossRef]
18. Deng, W.; Yuan, Z.; Liu, S.; Yang, Z.; Li, J.; Wang, E.; Wang, X.; Li, J. Plasmonic enhancement for high-efficiency planar heterojunction perovskite solar cells. *J. Power Sources* **2019**, *432*, 112–118. [CrossRef]
19. Fu, N.; Bao, Z.Y.; Zhang, Y.L.; Zhang, G.; Ke, S.; Lin, P.; Dai, J.; Huang, H.; Lei, D.Y. Panchromatic thin perovskite solar cells with broadband plasmonic absorption enhancement and efficient light scattering management by Au@Ag core-shell nanocuboids. *Nano Energy* **2017**, *41*, 654–664. [CrossRef]
20. Irandoost, R.; Soleimani-Amiri, S. Design and analysis of high efficiency perovskite solar cell with ZnO nanorods and plasmonic nanoparticles. *Optik Int. J. Light Electron Opt.* **2020**, *202*, 163598. [CrossRef]
21. Beck, F.; Mokkapati, S.; Catchpole, K. Light trapping with plasmonic particles: Beyond the dipole model. *Opt. Express* **2011**, *19*, 25230–25241. [CrossRef]
22. Saleh, Z.; Nasser, H.; Özkol, E.; Günöven, M.; Altuntas, B.; Bek, A.; Turan, R. Enhanced Optical Absorption and Spectral Photocurrent in a-Si: H by Single- and Double-Layer Silver Plasmonic Interfaces. *Plasmonics* **2014**, *9*, 357–365. [CrossRef]
23. Hajjiah, A.; Parmouneh, F.; Hadipour, A.; Jaysankar, M.; Aernouts, T. Light Management Enhancement for Four-Terminal Perovskite-Silicon Tandem Solar Cells: The Impact of the Optical Properties and Thickness of the Spacer Layer Between Sub-Cells. *Materials* **2018**, *11*, 2570. [CrossRef]
24. Sharma, R.K.; Hazdra, P.; Popelka, S.; Mihaila, A.; Bartolf, H. *Version 5.20.2.R, Software for Device Simulation Framework*; Silvaco Inc.: Santa Clara, CA, USA, 2020.
25. Sze, S.; Ng, K.K. *Physics of Semiconductor Devices*; John Wiley & Sons: Hoboken, NJ, USA, 2006.
26. Silvaco. Available online: https://dynamic.silvaco.com/dynamicweb/jsp/downloads/DownloadManualsAction.do?req=silen-manuals&nm=atlas (accessed on 22 April 2020).
27. Dewan, R.; Fischer, S.; Meyer-Rochow, V.B.; Özdemir, Y.; Hamraz, S.; Knipp, D. Studying Nanostructured Nipple Arrays of Moth Eye Facets Helps to Design Better Thin Film Solar Cells. *Bioinspir. Biomim.* **2011**, *7*, 016003. [CrossRef] [PubMed]
28. Lee, Y.J.; Ruby, D.S.; Peters, D.W.; McKenzie, B.B.; Hsu, J.W.P. ZnO Nanostructures as Efficient Antireflection Layers in Solar Cells. *Nano Lett.* **2008**, *8*, 1501–1505. [CrossRef] [PubMed]
29. Qarony, W.; Hossain, M.; Dewan, R.; Fischer, S.; Meyer-Rochow, V.; Salleo, A.; Knipp, D.; Tsang, Y. Approaching Perfect Light Incoupling in Perovskite and Silicon Thin Film Solar Cells by Moth Eye Surface Textures. *Adv. Theory Simul.* **2018**, *1*, 1800030. [CrossRef]
30. O'Shea, S. *Diffractive Optics Design, Fabrication, and Test*; SPIE Press: Bellingham, DC, USA, 2003; Volume 62.
31. Holman, Z.C.; Filipič, M.; Descoeudres, A.; Wolf, S.D.; Smole, F.; Topič, M.; Ballif, C. Infrared Light Management in High-Efficiency Silicon Heterojunction and Rear-Passivated Solar Cells. *J. Appl. Phys.* **2013**, *113*, 013107. [CrossRef]

32. Raoult, E.; Bodeux, R.; Jutteau, S.; Rives, S.; Yaiche, A.; Coutancier, D.; Rousset, J.; Collin, S. Optical characterizations and modelling of semitransparent perovskite solar cells for tandem applications. In Proceedings of the 36th European Photovoltaic Solar Energy Conference and Exhibition, Marseille, France, 9–13 September 2019; pp. 757–763.
33. Manzoor, S.; Häusele, J.; Bush, K.; Palmstrom, A.; Carpenter, J.; Yu, Z.; Bent, S.; Mcgehee, M.; Holman, Z. Optical Modeling of Wide-Bandgap Perovskite and Perovskite/Silicon Tandem Solar Cells Using Complex Refractive Indices for Arbitrary-Bandgap Perovskite Absorbers. *Opt. Express* **2018**, *26*, 27441. [CrossRef]
34. Filipič, M.; Löper, P.; Niesen, B.; Wolf, S.D.; Krč, J.; Ballif, C.; Topič, M. CH3NH3PbI3 perovskite/silicon tandem solar cells: Characterization based optical simulations. *Opt. Express* **2015**, *23*, A263. [CrossRef]
35. Chen, C.-W.; Hsiao, S.-Y.; Chen, C.-Y.; Kang, H.-W.; Huang, Z.-Y.; Lin, H.-W. Optical Properties of Organometal Halide Perovskite Thin Films and General Device Structure Design Rules for Perovskite Single and Tandem Solar Cells. *J. Mater. Chem. A* **2015**, *3*, 9152–9159. [CrossRef]
36. Minemoto, T.; Murata, M. Device Modeling of Perovskite Solar Cells Based on Structural Similarity with Thin Film Inorganic Semiconductor Solar Cells. *J. Appl. Phys.* **2014**, *116*, 054505. [CrossRef]
37. Mandadapu, U.; Thyagarajan, K.; Vedanayakam, S.V. Simulation and Analysis of Lead Based Perovskite Solar Cell Using SCAPS-1D. *Indian J. Sci. Technol.* **2017**, *10*, 1–8. [CrossRef]
38. Reenen, S.V.; Kemerink, M.; Snaith, H.J. Modeling Anomalous Hysteresis in Perovskite Solar Cells. *J. Phys. Chem. Lett.* **2015**, *6*, 3808–3814. [CrossRef] [PubMed]
39. Almosni, S.; Cojocaru, L.; Li, D.; Uchida, S.; Kubo, T.; Segawa, H. Tunneling-Assisted Trapping as One of The Possible Mechanisms for The Origin of Hysteresis in Perovskite Solar Cells. *Energy Technol.* **2017**, *5*, 1767–1774. [CrossRef]
40. Jaysankar, M.; Qiu, W.; Van Eerden, M.; Aernouts, T.; Gehlhaar, R.; Debucquoy, M.; Paetzold, U.W.; Poortmans, J. Four-Terminal Perovskite/Silicon Multijunction Solar Modules. *Adv. Energy Mater.* **2017**, *7*, 1602807. [CrossRef]
41. Minemoto, T.; Murata, M. Theoretical Analysis on Effect of Band Offsets in Perovskite Solar Cells. *Sol. Energy Mater. Sol. Cells* **2015**, *133*, 8–14. [CrossRef]
42. Mandadapu, U.; Vedanayakam, V.; Thyagarajan, K.; Reddy, M.R.; Babu, B.J. Design and Simulation of High Efficiency Tin Halide Perovskite Solar Cell. *Int. J. Renew. Energy Res.* **2017**, *7*, 1603–1612.
43. Du, H.-J.; Wang, W.-C.; Zhu, J.-Z. Device Simulation of Lead-Free CH3NH3SnI3 Perovskite Solar Cells with High Efficiency. *Chin. Phys. B* **2016**, *25*, 108802. [CrossRef]
44. Razzaq, A.; Depauw, V.; Cho, J.; Radhakrishnan, H.; Gordon, I.; Szlufcik, J.; Abdulraheem, Y.; Poortmans, J. Periodic Inverse Nanopyramid Gratings for Light Management in Silicon Heterojunction Devices and Comparison with Random Pyramid Texturing. *Sol. Energy Mater. Sol. Cells* **2020**, *206*, 110263. [CrossRef]
45. Carretero-Palacios, S.; Calvo, M.; Míguez, H. Absorption Enhancement in Organic–Inorganic Halide Perovskite Films with Embedded Plasmonic Gold Nanoparticles. *J. Phys. Chem. C* **2015**, *119*, 18635–18640. [CrossRef] [PubMed]
46. Guillemoles, J.-F.; Kirchartz, T.; Cahen, D.; Rau, U. Guide for the perplexed to the Shockley–Queisser model for solar cells. *Nat. Photonics* **2019**, *13*, 501–505. [CrossRef]